CrystEngComm

PAPER

View Article Online
View Journal | View Issue

Cite this: *CrystEngComm*, 2014, **16**, 7062

Evolution of ZnO microstructures from hexagonal disk to prismoid, prism and pyramid and their crystal facet-dependent gas sensing properties†

Nan Qin,[a] Qun Xiang,*[b] Hongbin Zhao,[b] Jincang Zhang[a] and Jiaqiang Xu*[bc]

Received 27th March 2014,
Accepted 11th June 2014

DOI: 10.1039/c4ce00637b

www.rsc.org/crystengcomm

Herein, the evolution of ZnO structures from hexagonal disk to prismoid, prism and pyramid was found *via* a facile two-step low temperature hydrothermal reaction, and the evolution was achieved by only adjusting the pH value of the reactive solution without the assistance of a template or a surfactant. The characterization results showed that the precursor (hexagonal $Zn_5(OH)_8Cl_2{\cdot}2H_2O$ disk) played a key role in the morphology evolution of ZnO during the early stage of the growth process and that the disks tended to stack together layer by layer in both directions (up and down) to form prismoid, prism and pyramid structures with the increase in pH value from 7 to 10. After calcination, the corresponding hexagonal ZnO microstructures were obtained. This structure evolution resulted in the weakening dominance of the (0001) plane in the total exposed crystal facets. Furthermore, despite the similar specific surface areas of the four hexagonal ZnO microstructures, the gas sensing properties of the sensors based on these microstructures deteriorated sequentially. At a working temperature of 330 °C, the ZnO disk with the most exposed (0001) plane showed the highest gas response toward ethanol, which was nearly 2, 3, and 6 times higher than those of the prismoid, prism and pyramid structures, respectively. This superior gas sensing performance strongly depends on the predominantly exposed polar facets (0001), which can provide more active sites for oxygen adsorption and subsequent reaction with the detected gas than other apolar facets. It demonstrates that the (0001) crystal facet plays a significant role in the gas sensing behavior of ZnO. This research will bring some inspiration to researchers for the fabrication of a high performance ZnO gas sensor as well as other metal oxides.

Introduction

As one of the important metal oxide semiconductor materials, zinc oxide (ZnO), with a wide bandgap of 3.37 eV and large exciton binding or Rydberg energy of ~60 meV, has been actively studied due to its excellent chemical/electrical/optical properties and easy growth of desired nanostructures for functional devices, such as sensors, solar cells, light emitting diodes, and ultraviolet lasers.[1–5] To date, ZnO micro/nanostructures such as zero-dimensional (0D) quantum dots;[6–8] one-dimensional (1D) nanorods,[9–11] nanowires[12–14] and nanotubes;[15] two-dimensional (2D) nanosheets[16] and nanobelts;[17] even three-dimensional (3D) nanoflowers[18] and hollow structures,[19] *etc.*, have all been prepared successfully by using either physical deposition or chemical methods.

In principle, gas sensing based on metal oxide semiconductors originates from the oxidation–reduction reaction occurring on the semiconductor surface between the detected gas and the chemisorbed oxygen, which leads to a resistance change on the sensor. For this reason, the sensitivity of the sensor depends on the surface atom structure of the exposed facets. Favorable exposed reactive surfaces are expected to be effective in promoting the chemical sorption of oxygen, thus enhancing gas sensitivity.[20] The most stable surfaces of wurtzite ZnO include the $\{10\bar{1}0\}$, $\{2\bar{1}10\}$ and $\{0001\}$ facets, of which the first two are non-polar and the last is polar. Typically, ZnO crystals with a hexagonal rod shape along the *c*-axis are conventionally achieved due to a large anisotropic growth rate (V) of the individual facet, $V_{[0001]} \gg V_{[01\bar{1}0]} > V_{[000\bar{1}]}$.[21–26] In fact, during the growth process, ZnO nanostructures tend to maximize the exposed areas of the apolar planes because of their low surface energies and tend to minimize the areas of the polar planes.[27] However, the ZnO structures with large polar (0001) surfaces receive special attention due to their enhanced catalytic[28,29] and photocatalytic

[a] *Department of Physics, College of Science, Shanghai University, Shanghai, 200444, China*
[b] *NEST Lab, Department of Chemistry, College of Science, Shanghai University, Shanghai, 200444, China. E-mail: xujiaqiang@shu.edu.cn; Tel: +86 21 66132701*
[c] *State Key Laboratory of Transducer Technology, Shanghai Institute of Microsystem and Information Technology, Chinese Academy of Sciences, Shanghai, 200050, China*

† Electronic supplementary information (ESI) available. See DOI: 10.1039/c4ce00637b

activities.[30,31] In the field of gas sensing, Liu[32] and Zhao[33] find that the enhanced gas sensing performance is dependent on the (0001) facets, while in the studies of Kaneti[34] and Xiao,[35] the (10$\bar{1}$0) facets show better gas sensing performance. The reason for this disagreement is associated with the difficulty in the controlled synthesis of ZnO with a comparable structure feature, such as a similar specific surface area and different exposed crystal facets at the same time. Up to now, solution-based methods have been successfully employed to control ZnO crystal growth through the use of organic agents, such as ethylenediamine,[36] citrates,[37] amino acids,[38] polyacrylamide,[39] sodium poly(styrenesulfonate), poly (diallyldimethylammonium chloride),[40] vitamin C,[41] diblock copolymers,[42] and gelatin.[43] It has been found that the absorption of organic molecules into the surfaces of ZnO during synthesis may influence the nucleation and growth of ZnO crystals.[44] However, organic additives are always expensive and harsh reaction conditions are also required. Actually, it is not easy to achieve good control of a ZnO structure with the desired crystal planes.

In this study, a facile two-step low temperature hydrothermal method is employed for the synthesis of ZnO microstructures with different exposing crystal planes by adjusting the pH value of the solution instead of using a template or a surfactant. With the increase in the pH value from 7 to 10, a ZnO hexagonal disk, a prismoid, a prism and a pyramid are obtained sequentially. The growth process is observed by FESEM in the form of stacking together layer by layer in both directions (up and down), arising from the initial small hexagonal disk. Meanwhile, the evolution of the crystal structure results in the weakening dominance of the (0001) facet in the total exposed surface. Through the gas-sensing test, we find that gas sensors based on various ZnO crystal microstructures exhibit distinct performances. The hexagonal disk-based sensor with the most exposed (0001) facet shows superior sensing property, while the other microstructures demonstrate degenerated performance in the order of prismoid > prism > pyramid.

Experimental section

Materials

All reagents employed were analytically pure and used as received without further purification from Shanghai Chemical Industrial Co. Ltd. (Shanghai, China) unless otherwise mentioned.

Synthesis of hexagonal ZnO disk, prismoid, prism and pyramid

Various ZnO structures were synthesized *via* a simple two-step low temperature hydrothermal method.

Step 1: 10 mL of 0.2726 g $ZnCl_2$ and 10 mL of 0.2804 g hexamethylenetetramine aqueous solutions were mixed in a 50 mL Teflon-lined autoclave container and kept at 60 °C in a hot water bath for 15 min.

Step 2: a 15 mL mixed solution of 0.878 g of Zn $(CH_3COO)_2{\cdot}2H_2O$ and 0.5608 g of hexamethylenetetramine was then added into the container. The pH value of the mixed solution was adjusted to a range of 7–10 by adding a small quantity of ammonia solution. The Teflon-lined stainless steel autoclave with the solution was sealed and kept at 95 °C for 2 h. After the reaction, a white powder was found at the bottom of the container. The powder was rinsed with deionized water and ethanol several times and then dried at 80 °C for 10 h. At last, the final product was obtained through heat treatment at 500 °C for 1 h.

Characterization

The crystal phase of the product was determined by powder X-ray diffraction (XRD) analysis using a DX-2700 diffractometer with Cu Kα_1 radiation (λ = 1.54056 Å) (Haoyuan, Dandong, China), and the XRD data were collected at a scanning rate of 0.03 deg s^{-1} for 2θ ranging from 10° to 80°. Fourier transform infrared (FT-IR) spectra were confirmed with a spectrophotometer (FT-IR, Nicolet Avatar 370). The morphology of all the ZnO microstructures was observed by using a field emission scanning electron microscope (FESEM, JSM-6700F), a transmission electron microscope (TEM, JEM-200CX) and a high-resolution transmission electron microscope (HRTEM, JEM-2010, JEOL) with selected-area electron diffraction (SAED). Room temperature photoluminescence (PL) measurements were conducted on a Hitachi RF-5301PC spectrofluorophotometer using a 350 nm Xe laser line as the excitation source. The specific surface area was estimated using the Brunauer–Emmett–Teller (BET) equation based on the nitrogen adsorption isotherm (77 K) by using a 3H-2000III surface area analyzer (Shanghai Xiehe Industry Co., Ltd.).

Fabrication and response test of the gas sensor

Referring to our previous work,[45] like the schematic drawing of the as-fabricated gas sensor shown in Fig. 1a, ZnO powder

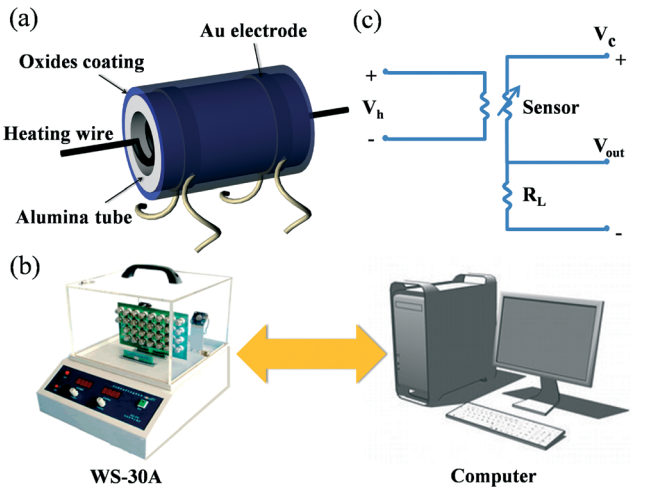

Fig. 1 (a) Sketch of the gas sensor. (b) Setup of the gas sensing test system. (c) Electric circuit of the gas sensing test.

and terpineol were ground together in an agate mortar to form a paste. Then the paste was coated on an alumina tube on which a pair of Au electrodes had been printed previously, followed by drying at 100 °C for 2 h and subsequent annealing at 500 °C for 2 h. Finally, a small Ni–Cr alloy coil was inserted into the tube as a heater so as to adjust and optimize the working temperature of the gas sensor.

To improve the long-term stability, the sensors were kept at the working temperature for several days. As shown in Fig. 1b, the test was operated in an HW-30A measuring system (Hanwei Electronics Co. Ltd., P.R. China). All the gas sensing measurements were carried out in ambient air with a humidity of about 40% and the chamber temperature was about 30 °C. The details of the gas concentration calculations are shown in the ESI.† A stationary state gas distribution method was used for testing the gas response.

Before the injection of a test gas or liquid, the test chamber was covered and filled with air. Keeping the fan of the measurement system working would favor the diffusion of the air. Under this working temperature, we could get the resistance of the sensor in the air (R_a). After the injection (the gas was immediately injected into the test chamber and mixed with air; the liquid should first be injected into the evaporator through a hole at the back of the chamber to convert it to its vapor phase and then mixed with air), the test chamber was kept covered. Meanwhile, the resistance of the sensor changed and reached a stable value several seconds later, and then the resistance of the sensor in the test gas (R_g) was recorded. When the test chamber was opened, the sensor was in contact with air again, and the resistance of the sensor would return to the level before the gas injection.

In the electric circuit for measuring gas response (Fig. 1c), a load resistor (R_L, 1 MΩ) was connected in series with a gas sensor. The circuit voltage (V_c) was set at 5 V, and the output voltage (V_{out}) was the terminal voltage of the load resistor. The working temperature of the sensor was adjusted by varying the heating voltage (V_h). The resistance of the sensor in air (R_a) or test gas (R_g) was measured by monitoring V_{out}. The gas response of the sensor in this paper was defined as R_a/R_g (reducing gases) or R_g/R_a (oxidizing gases). The response or recovery time was expressed as the time taken for the sensor output to reach 90% of its saturation after applying or switching off the gas in a step function.

Results and discussion

Structure and morphology of ZnO powders

The XRD patterns of the obtained precursor in step 1 and as-synthesized products (after calcination) are shown in Fig. 2. Obviously, as shown in the patterns, all diffraction peaks corresponding to the precursor obtained from step 1 are ascribed to the structure of zinc chloride hydroxide hydrate (simonkolleite, $Zn_5(OH)_8Cl_2{\cdot}2H_2O$) (JCPDS 07-0155) with lattice constants a and c of about 6.34 Å and 23.66 Å, respectively, and space group $R3m$. In view of the intensity of the (003) Bragg peak, this $Zn_5(OH)_8Cl_2{\cdot}2H_2O$ precursor has a

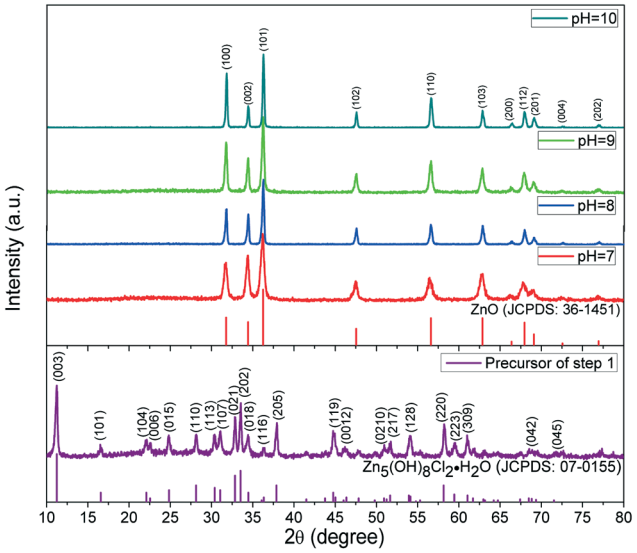

Fig. 2 XRD patterns of the precursor in step 1 and as-synthesized products (after calcination).

strong preferential orientation along (003).[46] Besides, the XRD patterns of the products obtained from various pH values (after calcination) are indexed to the wurtzite ZnO (JCPDS 36-1451) structure with the lattice constants a = 3.25 Å and c = 5.207 Å, implying that the product has a high degree of crystallization and high purity. However, the diffraction intensity ratio of the (0001) plane to the (10$\bar{1}$0) plane ($I_{(0002)}/I_{(10\bar{1}0)}$) gradually becomes weaker with the increase in pH value. A higher $I_{(0002)}/I_{(10\bar{1}0)}$ value means a larger fraction of the (0001) plane, indicating that the exposure of the (0001) plane is dominant.[47] The calculated values of average crystallite sizes in the [0001] and [10$\bar{1}$0] directions are listed in Table 1. It can be seen that crystallite growth occurs with the increase in pH value. When the pH value is about 7, the extracted crystallite size in the [10$\bar{1}$0] direction is larger in comparison to that in the [0001] direction, implying that the shape of the crystallites is disk-like. When the pH value was further increased from 8 to 10, the crystallite size in the [10$\bar{1}$0] direction was smaller than that in the [0001] direction, indicating that the shape of the crystallites is rod-like. The rod axis is along the [0001] direction.[11]

Fig. 3 depicts a typical Fourier transform infrared (FT-IR) spectrum from the precursor obtained from step 1 and the hexagonal ZnO disk in the spectral region of 4000–400 cm^{-1}. The strong band at 1607 cm^{-1} is due to the deformation

Table 1 Morphological features of the synthesized ZnO products

Sample	Average crystallite size in *hkl* direction/nm	
	$D_{(10\bar{1}0)}$	$D_{(0001)}$
pH = 7	21.1	17.2
pH = 8	24.8	29.6
pH = 9	28.1	37.5
pH = 10	33.8	43.7

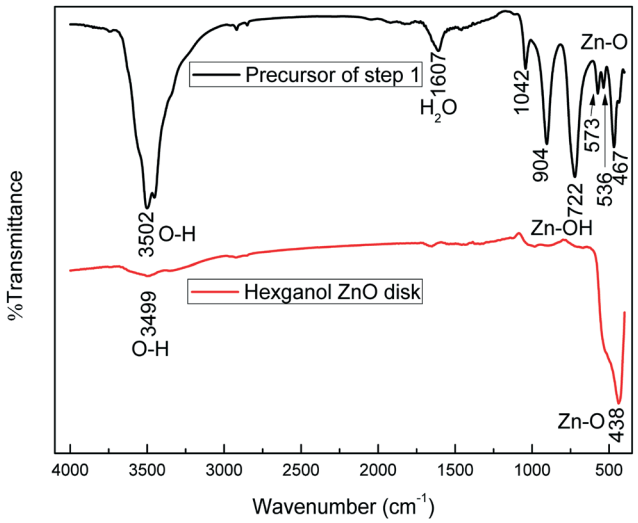

Fig. 3 Fourier transform infrared (FT-IR) spectrum of the precursor from step 1 and the hexagonal ZnO disk.

vibration of H_2O molecules, and the bands centered at 3499 and 3502 cm^{-1} are characteristic of O–H stretching vibration. Moreover, specific bands attributed to various stretching vibration modes of the chloride ion are observed at lower wavenumbers.[48–50] Two bands at 904 and 722 cm^{-1} are assigned to Zn–OH vibrations. The obtained ZnO is further confirmed by the bands in the 350–600 cm^{-1} region, which correspond to translational modes of the Zn–O bonds.[46,51]

Fig. 4a shows a typical FESEM image of the precursor obtained from step 1 (simonkolleite). It can be clearly seen that the precursor has a hexagonal disk shape with a diameter of about 1 μm, and the disk is so transparent that a thin and single- or few-layer structure can be found. Fig. 4b presents the FESEM image of the precursor from step 2 (pH = 7). Compared with the precursor from step 1, the hexagonal disk multilayer structure was obtained after the hydrothermal process. It consists of several larger hexagonal disks with diameters in the range of 1–10 μm stacking with each other in both directions (up and down), which can be further determined from the enlarged top and side view FESEM images of a single multilayer structure (Fig. 4b, inset). Fig. 4c and d exhibit the FESEM images of the hexagonal ZnO disk after the heat treatment. It is worth noting that the interesting multilayer structure inherited from the precursor is well maintained. In Fig. 4d, the enlarged side view of an individual hexagonal ZnO disk demonstrates that porous structures are formed. The size of the pore dispersed in this material, with a diameter of about tens of nanometers, can be confirmed from the TEM image (as shown in Fig. 4e). The thickness of the disk is measured to be about 100 nm, as shown in the upper left inset (Fig. 4d) of the high magnification cross-sectional view of the hexagonal disk. Fig. 4f presents the HRTEM image of the hexagonal disk. The 2D lattice fringe spacing is measured to be about 0.28 nm, with an angle of about 60°, corresponding to the $\{10\bar{1}0\}$ crystal planes of wurtzite ZnO. The SAED pattern shown in the inset can be indexed as the [0001] zone axis of single-crystalline ZnO with a hexagonal structure. The SAED and HRTEM results indicate that the disk grew mainly along the six symmetric directions perpendicular to $(10\bar{1}0)$, $(\bar{1}010)$, $(01\bar{1}0)$, $(0\bar{1}10)$, $(\bar{1}100)$ and $(1\bar{1}00)$ facets and are enclosed by ±(0001) top and bottom surfaces.

In this study, we focus on the controllable synthesis of ZnO structures with different exposed crystal facets and investigate the effect of the exposed facets on the gas sensing property. Fortunately, we successfully obtained a series of

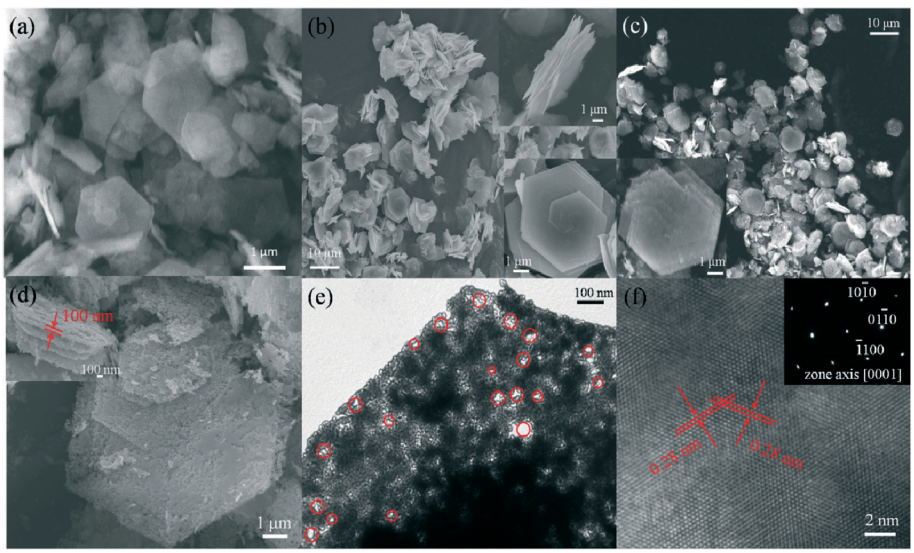

Fig. 4 FESEM images of (a) the precursor from step 1 (simonkolleite) and (b) the precursor from step 2 (pH = 7); the upper right and lower right insets are the enlarged side and top views of a single hexagonal disk, respectively. (c and d) ZnO hexagonal disk after the heat treatment (pH = 7); the lower left inset of (c) and the upper left inset of (d) are the enlarged top and side views of a single hexagonal disk, respectively. (e) TEM image (the red circles indicate the pores in the hexagonal disk structure) and (f) HRTEM image of the hexagonal ZnO disk (pH = 7); the inset is the corresponding SAED pattern.

ZnO microstructures with different exposed facets by simply adjusting the pH of the solution. Fig. 5 displays the FESEM images of ZnO products corresponding to the pH value from 8 to 10. In Fig. 5a and b, when the pH value was about 8, a hexagonal ZnO prismoid could be observed with a diameter of about 1.5 μm and a length of about 2 μm. Interestingly, this prismoid structure is composed of two sections, and some disk-like structures can be seen from the enlarged top view. Fig. 5c and d are the FESEM images of the obtained hexagonal ZnO prism, when the pH value of the solution was about 9. The diameter and the length of the prism are about 1 μm and 5 μm, respectively. This prism structure is also divided into two parts from the middle, which is similar to the previous prismoid structure. Moreover, as clearly shown in Fig. 5d, some disk fractions remain on the top of the hexagonal prism. Finally, with the continuing increase in the pH value up to about 10, a hexagonal ZnO pyramid was formed with a diameter of about 1 μm and a length of about 5 μm, as depicted in Fig. 5e and f. Especially in Fig. 5f, the top view of the hexagonal pyramid reveals that multilayer hexagonal disks stack together one by one in an orderly manner from small to large and then to small. In this way, the formation of the hexagonal bipyramid structure is achieved.

On the basis of the reactants used in the synthesis process and the characterization above, a possible formation mechanism of the structure evolution (a) and the crystal facets in hexagonal ZnO structures (b) are illustrated in Fig. 6. At first, the generation of simonkolleite ($Zn_5(OH)_8Cl_2{\cdot}2H_2O$) hexagonal disks was considered to proceed competitively in the solution following the successive chemical reactions:[52]

$$C_6H_{12}N_4 + 6H_2O \rightarrow 6HCHO + 4NH_3 \quad (1)$$

$$NH_3 + H_2O \rightarrow NH_4^+ + OH^- \quad (2)$$

$$ZnCl_2 + H_2O \rightarrow Zn(OH)_2 + 2HCl \quad (3)$$

$$Zn(OH)_2 \leftrightarrow Zn^{2+} + 2OH^- \quad (4)$$

$$HCl \rightarrow H^+ + Cl^- \quad (5)$$

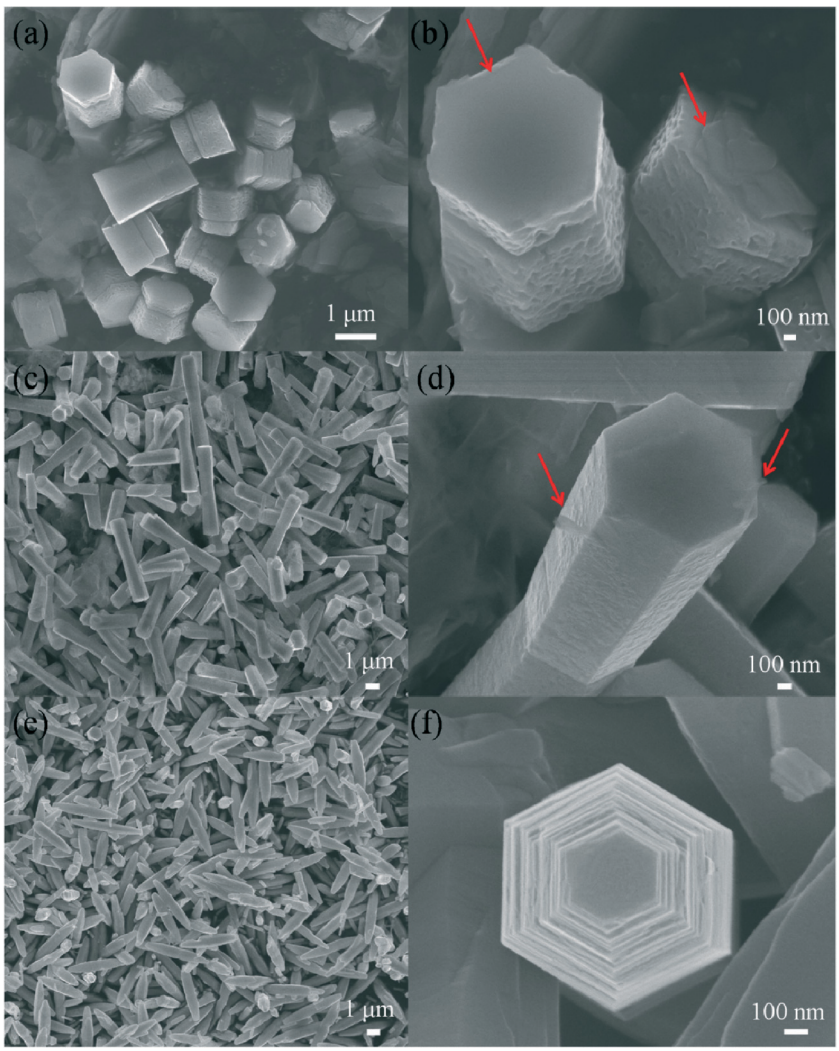

Fig. 5 FESEM images of various hexagonal ZnO microstructures corresponding to pH = 8 (a and b), pH = 9 (c and d) and pH = 10 (e and f).

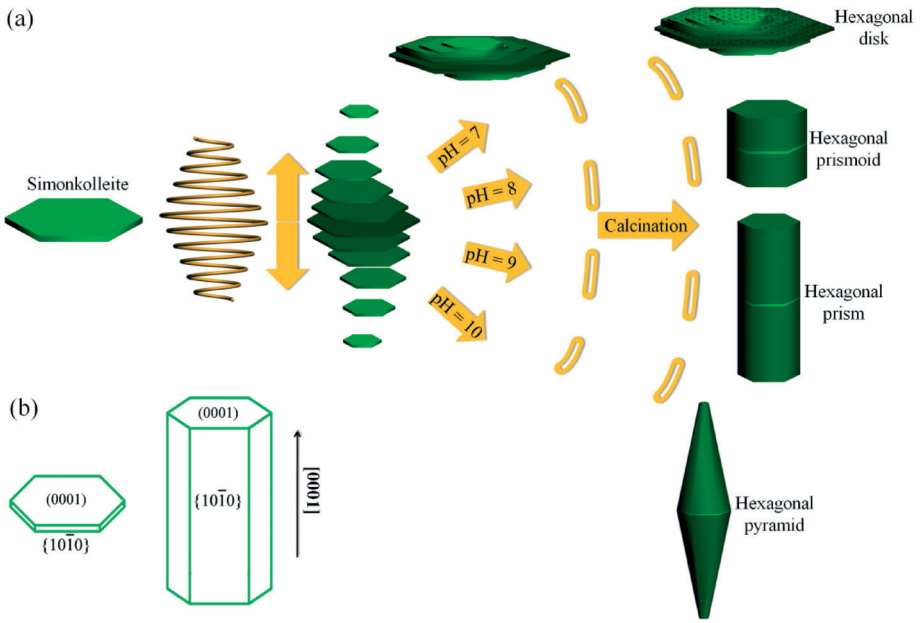

Fig. 6 Illustration of (a) the formation mechanism of various hexagonal ZnO structures and (b) the crystal facets in hexagonal ZnO structures.

$$5Zn^{2+} + 8OH^- + 2Cl^- + 2H_2O \rightarrow Zn_5(OH)_8Cl_2{\cdot}2H_2O \quad (6)$$

First, $C_6H_{12}N_4$ decomposes into formaldehyde (HCHO) and ammonia (NH_3) as shown in eqn (1). Ammonia forms ammonium hydroxide in water to produce OH^- anions (eqn (2)). Secondly, zinc chloride hydrolyzes in water and the products decompose into zinc ion (Zn^{2+}) and chloride anion (Cl^-) (eqn (3)–(5)). Finally, OH^- and Cl^- anions react with Zn^{2+} cations to synthesize hexagonal simonkolleite disks (eqn (6)).

At high temperature (500 °C), $Zn_5(OH)_8Cl_2{\cdot}2H_2O$ decomposed completely to form ZnO:[53]

$$Zn_5(OH)_8Cl_2{\cdot}2H_2O \rightarrow 5ZnO + 5H_2O + 2HCl \quad (7)$$

It is found that the formation of simonkolleite disks obviously occurs in a hydrothermal system with the combination of lower alkalinity, lower temperature (<100 °C), higher NH_4^+ ion concentration and existence of a Cl^- anion. Since simonkolleite has perfect cleavages parallel to the (0001) plane, there may be a direct interaction with some ligands on the exposed Zn surface. One Zn site is coordinated by six OH groups in an octahedral arrangement and the other Zn site is coordinated by three OH groups and one Cl atom in a tetrahedral arrangement in the simonkolleite structure. Here, Cl^- must be an acceptor anion for several hydrogen bonds to satisfy its bond-valence requirements of simonkolleite disks.[49] The simonkolleite disks cannot aggregate with each other along the biggest face (basal plane) due to the multi-interaction of its non-polarity, the perfect (0001) cleavage and the absorption of numerous Cl^- and OH^- ions on the basal (0001) plane. Furthermore, polar faces with surface dipoles are thermodynamically less stable than non-polar faces, which tend to rearrange themselves to minimize surface energy.[54] Hence, stacking together along [0001] and [000$\bar{1}$] directions for the simonkolleite disks is a preferred choice. With the addition of the nutrient solution in step 2, the hexagonal disks grew larger and a multilayer structure was obtained at the pH value of about 7. When the pH value of the solution increased to 8 and 9, there was an abundance of Zn^{2+} and OH^-. More and more disks gathered spontaneously and rapidly to form the dense hexagonal prismoid and prism structure with a large *c*-axis length and a small diameter. When the pH value reached about 10, excessive OH^- led to the dissolution of the polar faces, and finally the hexagonal pyramid was achieved. The high magnification views of the disk fractions on the top of various structures (as shown in Fig. 5b, d and f) provide a strong evidence of the abovementioned stacking behavior along the [0001] and [000$\bar{1}$] directions. Obviously, the evolution of the structures brought about the weakening dominance of the polar facets

Table 2 BET surface areas and estimated percentages of the (0001) facet in the total surface of ZnO hexagonal microstructures

	Hexagonal disk	Hexagonal prismoid	Hexagonal prism	Hexagonal pyramid
Average diameter (μm)	5.00	1.50	1.00	0.50 (end) 1.00 (middle)
Average thickness (μm)	0.10	2.00	5.00	5.00
BET surface area ($m^2\ g^{-1}$)	6.38	5.65	4.98	4.63
Calculated percentage of (0001) face (%)	47.8	12.3	4.00	1.40

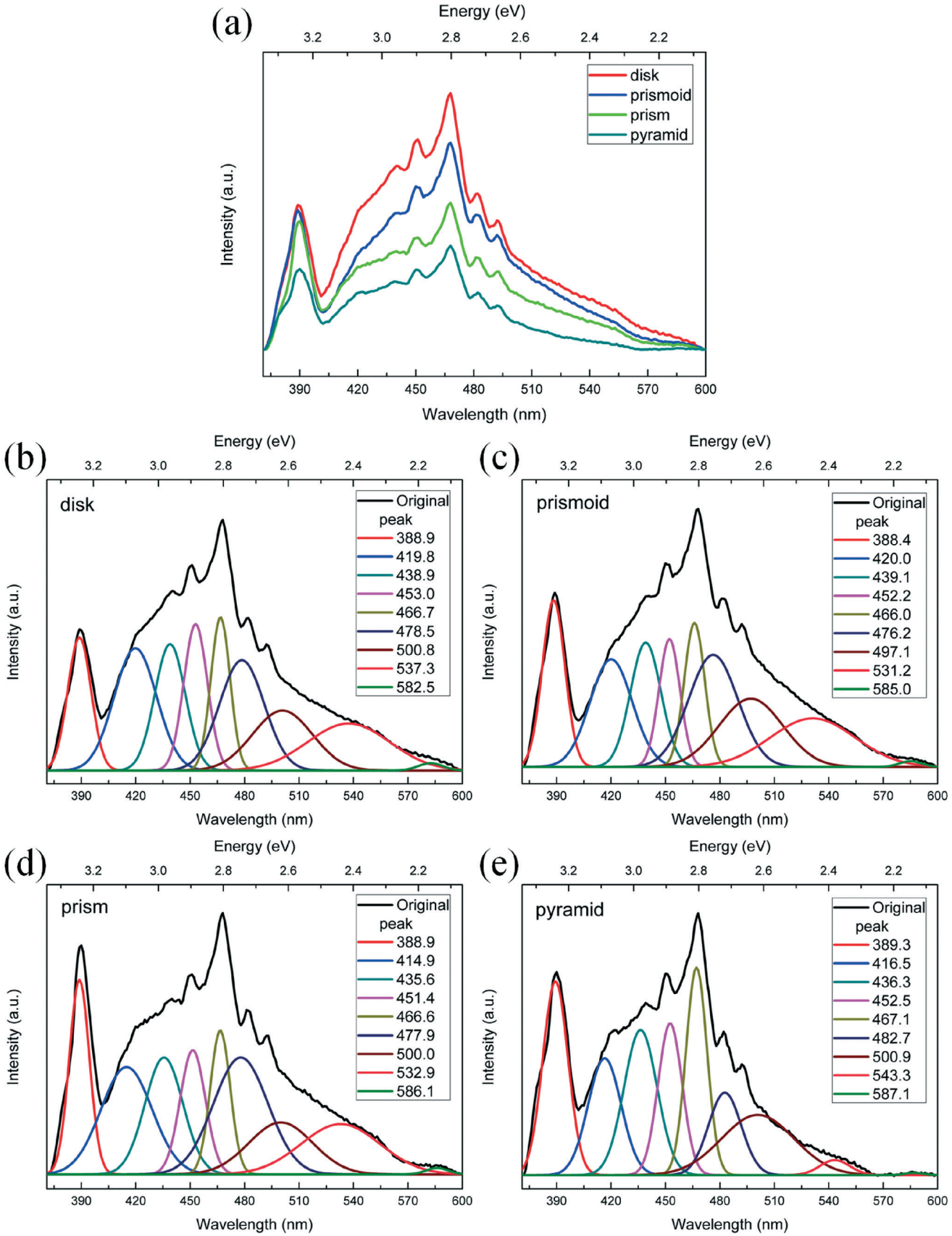

Fig. 7 Room temperature PL spectra and the corresponding Gaussian deconvolutions of the as-synthesized hexagonal ZnO microstructures recorded using an excitation wavelength of 350 nm.

(0001) in the total exposed surface to guarantee the minimum surface energy. The BET surface areas and theoretical percentages of the (0001) facet in the total surface corresponding to four different samples estimated from the FESEM results are summarized in Table 2.

Native defects of ZnO are associated with the gas sensing property. PL is an effective way to study the defect structure of semiconductor metal oxides.[55,56] There are generally believed to be six intrinsic defects in ZnO: interstitial zinc (Zn_i), zinc vacancy (V_{Zn}), Zn antisite (Zn_O), oxygen vacancy (V_O), interstitial oxygen (O_i), and oxygen antisite (O_{Zn}).[57] Fig. 7(a)–(e) present the Gaussian deconvolutions of the PL spectra for the as-synthesized ZnO products. According to their origin, the ultraviolet (UV) peak at ~3.2 eV (~385 nm) is assigned to the exciton emission from conduction band to valence band (CB–VB);[58] the peaks at ~2.9 eV (~415, ~435 and ~450 nm) are attributed to Zn_i;[59] the peaks at ~2.7 eV (~465 and ~475 nm) are assigned to V_{Zn};[60] the peak at ~2.53 eV (~500 nm) is attributed to V_O;[61] the emission at ~2.36 eV (~525 nm) is assigned to O_{Zn},[62] and the yellow and orange luminescence (>540 nm) is ascribed to O_i.[63] Defect percentages of the as-synthesized ZnO products are summarized in Table 3. Obviously, the hexagonal ZnO disk with the most exposed (0001) facet has a larger quantity of oxygen vacancies than the other three microstructures. Furthermore, the quantity of oxygen vacancies decreases, following the reduced percentage of the exposed (0001) facet. This indicates that the (0001) facet is strongly associated with the oxygen vacancy in ZnO, which is consistent with the previous studies.[64,65]

Gas sensing properties of the sensors

The gas-sensing properties of the sensors based on the as-synthesized ZnO microstructures are investigated, and the responses of all sensors upon exposure to 50 ppm ethanol at different operating temperatures are displayed in Fig. 8a. Clearly, the responses of all sensors increase abruptly at first and then decrease with increasing operating temperature. The optimum operating temperature is 330 °C. Therefore, the temperature of 330 °C was chosen for further examination of the gas sensing characteristics of all sensors. H_2, NO_x, CO, HCHO, CH_3OH, and NH_3 were also selected as target gases for the gas sensing detection. Fig. 8b shows the responses of all sensors toward these various gases (gas concentration 50 ppm) at the optimum working temperature of 330 °C. Obviously, the response to ethanol is significantly higher than the response to the other gases, revealing a more satisfactory selectivity for ethanol of all sensors.

Fig. 9a exhibits the response and recovery curves of all sensors upon exposure to 1, 3, 5, 10, 30, 50, 100, 200 and 500 ppm ethanol at the optimum operating temperature. Fig. 9b shows the relationship between response and ethanol concentration. It can be clearly seen that the response of the sensors toward ethanol reduces dramatically, associated with the evolution of the microstructures from hexagonal disk to prismoid, prism and pyramid. For example, their responses to 50 ppm ethanol are 87.4 (disk), 29.3 (prismoid), 21.6 (prism) and 13.3 (pyramid), respectively. The response of the ZnO disk-based gas sensor to ethanol is nearly 6 times higher than that of the pyramid-based sensor. Moreover, even though the ethanol concentration is down to 1 ppm, it can still be detected by the sensor based on the ZnO disk with a response of about 3.6, while the responses of the other sensors are no more than 2. Since the surface areas of these four hexagonal structures are similar, the distinct gas sensing properties may be caused by the various percentages of the exposed crystal facets in the entire surface. Apparently, the more the polar facet (0001) is exposed, the higher the gas

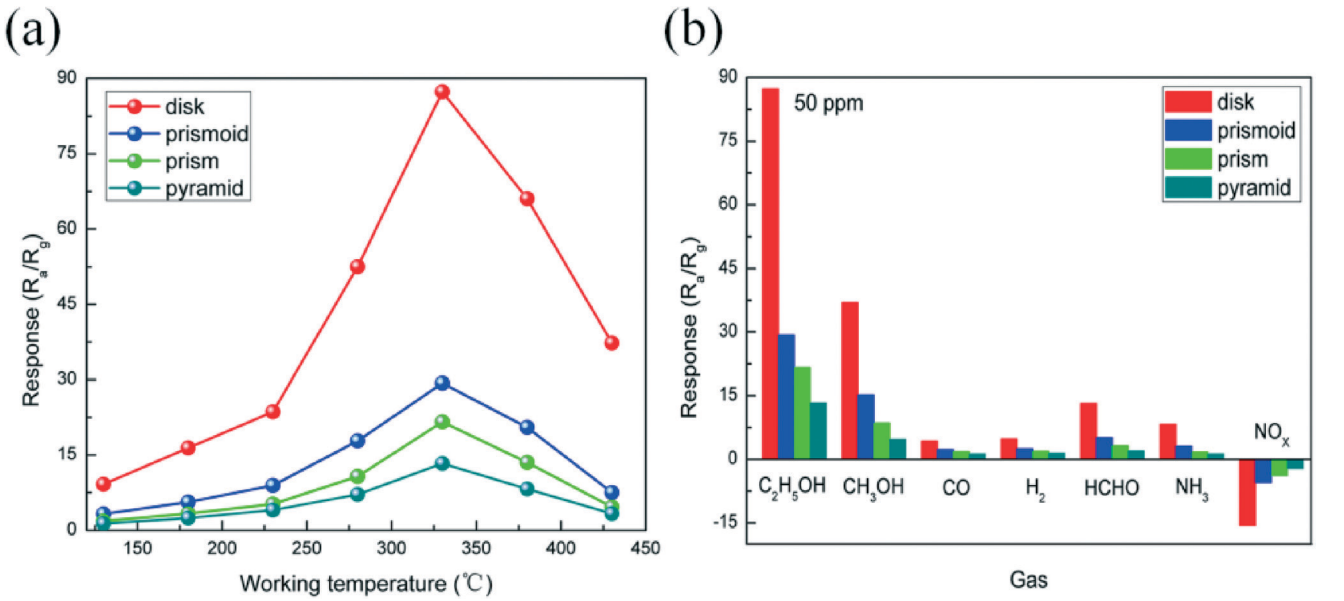

Fig. 8 (a) Relationship between the response and the working temperature of the sensors to 50 ppm ethanol vapor. (b) Gas response of the sensors to 50 ppm various gases at the optimum working temperature of 330 °C.

Table 3 Defect percentages of the as-synthesized hexagonal ZnO microstructures calculated by their corresponding PL spectra

Origin	Peak (nm)	Disk (%)	Prismoid (%)	Prism (%)	Pyramid (%)
(CB–VB) combination	~385	10.0	12.8	14.6	25.8
Zn_i (~2.9 eV)	~415, ~435, ~450	40.2	34.6	35.0	33.3
V_{Zn} (~2.7 eV)	~465, ~475	24.3	26.6	27.5	28.4
V_O (~2.53 eV)	~500	14.5	12.7	10.8	8.2
O_{Zn} (~2.36 eV)	~525	10.4	12.9	11.7	4.1
O_i (~2.13 eV)	~580	0.6	0.4	0.4	0.2

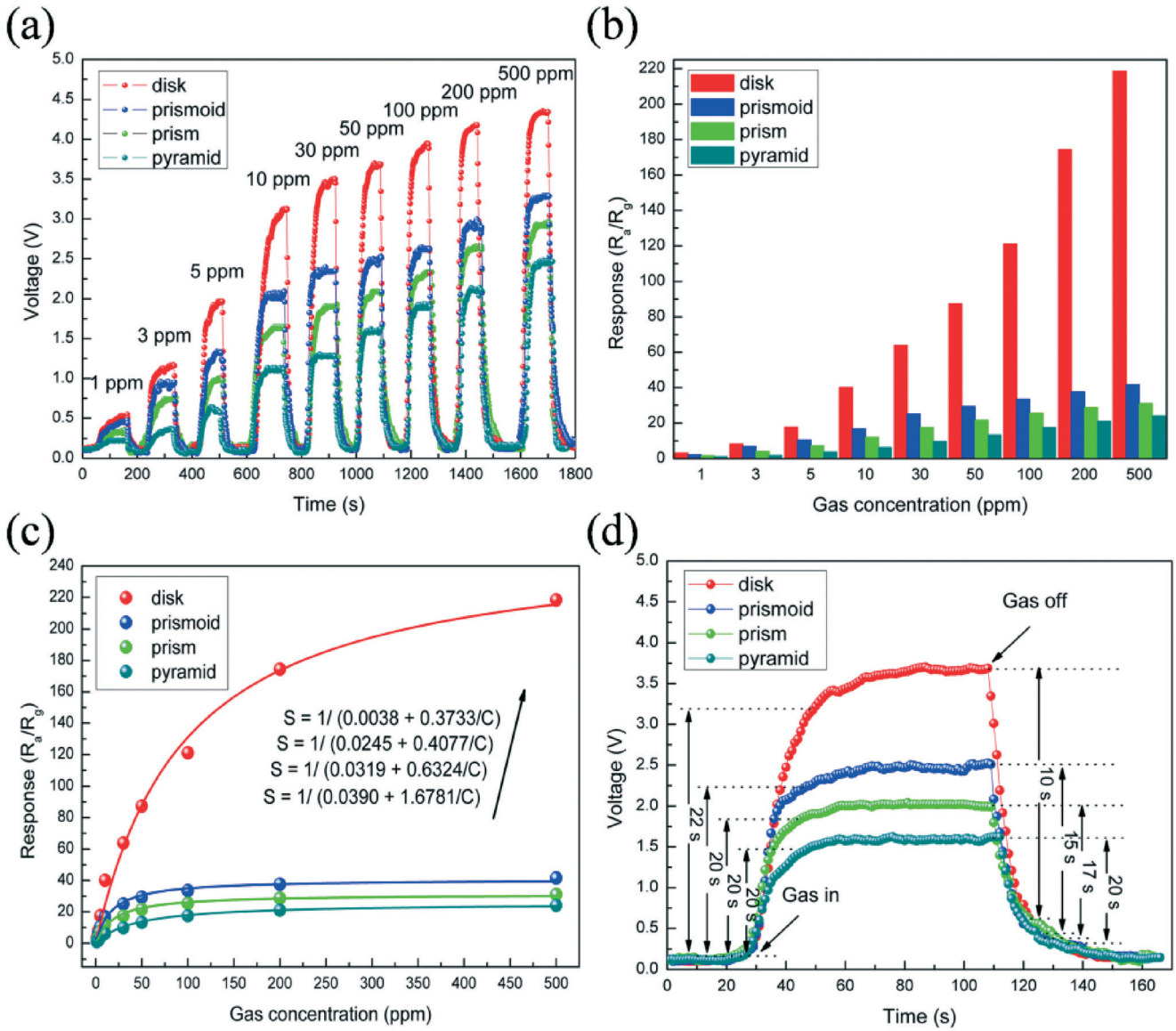

Fig. 9 (a) Dynamic sensing characteristics of the sensors towards ethanol vapor of various concentrations. (b) The corresponding response of the sensors. (c) Response of the sensors (*S*) *vs.* ethanol concentrations (*C*). (d) Response–recovery curve of the sensors to 50 ppm ethanol vapor.

sensing response would be generated. Accordingly, the better gas sensing property mainly depends on the more exposed (0001) facet. The gas response (R) as a function of ethanol concentration (C) is displayed in Fig. 9c, which was well fitted by using the equation $S = 1/(A + B/C)$. This can be understood as the surface coverage of adsorbed molecules followed the Langmuir isotherm model. At lower concentration, the sensor exhibits a linear dependence between the sensor response and the ethanol concentration. At higher concentration, the surface coverage tends to saturate and hence leads to the saturation response.[66,67] Fig. 9d displays the enlarged response–recovery curves of the sensors toward

50 ppm ethanol. It can be found that the response time of all sensors is about 20 s, while the recovery time increases from 10 s to 15 s, 17 s and 20 s, accordingly.

In general, the gas sensing mechanism for most metal oxide semiconductors can be ascribed to the change in the electrical conductivity arising from the chemical interaction between the gas molecules and the chemisorbed oxygen species on the surface of the sensing materials, as represented by Fig. 10a. The sensing process mainly involves the gas adsorption, charge transfer, and gas desorption.[68] Because the lower edge of the conduction band of ZnO (about 4.3 eV below the vacuum energy) is higher than the chemical potential of O_2 (about 5.7 eV below the vacuum energy),[69] when the ZnO sensors are exposed to air, oxygen molecules will be chemisorbed on the ZnO surface in the form of O_2^-, O^- and O^{2-} by capturing free electrons from the conduction band of ZnO. Then, ZnO shows a high resistance state in air due to the formation of a rather thick electron depletion region. It is worth noting that the existing form of chemisorbed oxygen species will change from O_2^-, O^- to O^{2-} with the increase in the working temperature. O_2^- is commonly chemisorbed at temperatures lower than 130 °C. However, at higher temperatures, O^- and O^{2-} are normally chemisorbed, while O^{2-} disappears rapidly.[70] In our case, at a working temperature of about 300 °C, O^- will play an important role in the gas sensing process.[71,72] The reaction kinetics can be described as eqn (3)–(6) in the ESI.†[73]

It is widely known that the (0001) polar plane of ZnO contains more oxygen vacancies than other facets and it is also proved by the PL characterization in this study.[64,65] These oxygen vacancies can significantly enhance the oxygen molecular adsorption and promote the dissociative adsorption, in which one of the oxygen atoms fills the original oxygen vacancy, while the other forms a bridging oxygen adatom between two Zn atoms,[71,74] as expressed by eqn (7) or (8) shown in the ESI.†[75] Moreover, for hexagonal ZnO, Zn atoms on the surface are usually coordinatively unsaturated, while the Zn and O atoms in the bulk are 4-fold coordinated. As shown in Fig. 10b, on the (0001) surface, all Zn atoms are coordinatively unsaturated, located in 3-fold coordinated sites with one dangling bond and in 2-fold coordinated sites with two dangling bonds. The $\{10\bar{1}0\}$ surface contains rows of 4-fold-coordinated Zn atoms and 3-fold-coordinated Zn atoms with one dangling bond perpendicular to the surface,[65,76] and hence more dangling bonds exist on the (0001) surface than on the $\{10\bar{1}0\}$ surface. It can be inferred that, because of the high activity, the adsorption of ionized oxygen species is more likely to occur on the (0001) plane of hexagonal ZnO rather than on other planes. For this reason, there will be more oxygen species on the (0001) polar plane than on $\{10\bar{1}0\}$ apolar planes, and thus the gas sensor based on hexagonal ZnO disks predominantly exposed with (0001) facet shows better gas-sensing properties than other sensors based on the hexagonal ZnO prismoid, prism and pyramid with more exposed $\{10\bar{1}0\}$ facets.

In addition, the C_2H_5OH gas can be either dehydrated at the surface of acidic oxide or dehydrogenated at the surface of basic oxide, as shown in eqn (9) or (10) in the ESI.†[72,77,78] Since ZnO is a basic metal oxide, the catalytic oxidation of C_2H_5OH on the ZnO surface will occur according to eqn (10)

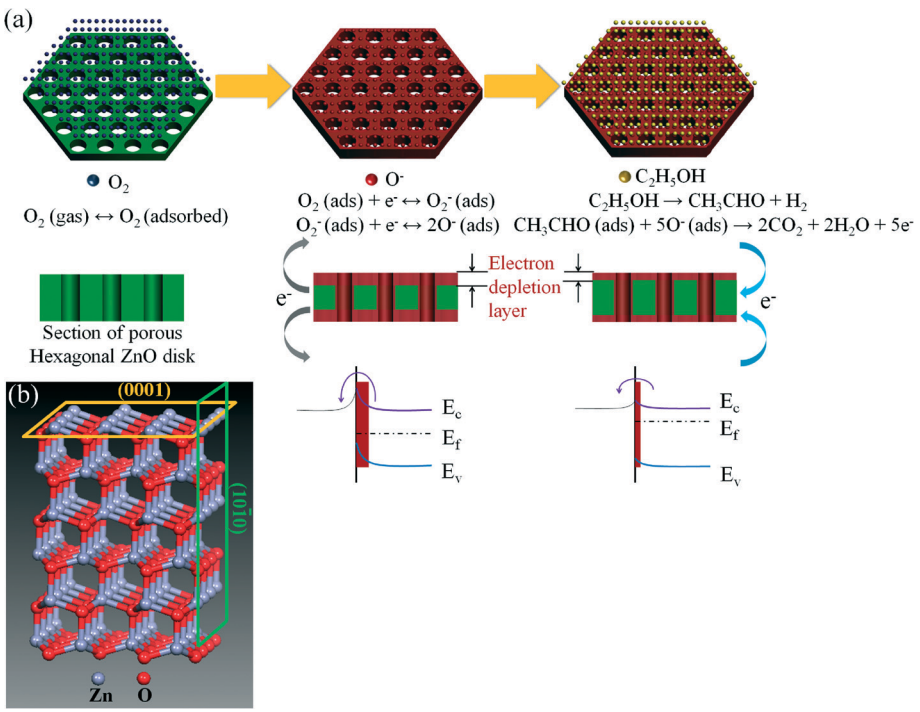

Fig. 10 Sketch of (a) the possible ethanol sensing process on the hexagonal ZnO disk-based sensor and (b) atomic model of wurtzite ZnO, clearly showing (0001) and $(10\bar{1}0)$ facets.

(ESI†). The sequential gas sensing reactions are shown in eqn (11)–(14) (ESI†). Obviously, the more the O^- is consumed, the more the electrons will be generated and released back to the conduction band of ZnO. An ethanol molecule leads to the release of 5 e^- back to the conduction band, which would reduce the depletion layer, further causing the sharp change in the sensor resistance among all the tested gases. Therefore, benefiting from the excellent electron transferring efficiency of the ethanol sensing reaction, the ZnO sensor always exhibits a very good ethanol sensing response than other gases.

Conclusions

In this paper, a hexagonal ZnO disk, a prismoid, a prism and a pyramid are successfully obtained through a simple two-step hydrothermal method from a hexagonal simonkolleite disk precursor by adjusting the pH value of the solution. The precursor disks are suggested to stack with each other along the [0001] and [000$\bar{1}$] directions. With the evolution of the structures, less (0001) crystal planes are exposed on the total surface. The gas sensing properties of these structures are degraded dramatically as well. At the working temperature of 330 °C, the response of the sensor based on the hexagonal ZnO disk toward 50 ppm ethanol is nearly 2, 3, and 6 times higher than that of the sensors based on hexagonal prismoid, prism and pyramid, respectively. This superior gas sensing performance strongly depends on the exposed crystal plane with the polar facets of (0001). The exposed (0001) facets of ZnO crystal structure can provide more active sites for oxygen adsorption and subsequent reaction with the detected gas than other apolar facets and thus increase the gas sensing response. The results demonstrate that it is a significant and promising method to control the exposed facet of a ZnO crystal structure for the fabrication of a high performance gas sensor.

Acknowledgements

This work was supported by the National Natural Science Foundation of China (no. 61371021) and Natural Science Foundation of Shanghai (no. 11ZR1412600). The authors thank the staff of the Instrumental Analysis and Research Center in Shanghai University for their help in material characterization.

References

1 O. Lupan, G. Chai and L. Chow, *Microelectron. Eng.*, 2008, **85**, 2220–2225.
2 M. T. Lloyd, R. P. Prasankumar, M. B. Sinclair, A. C. Mayer, D. C. Olson and J. W. Hsu, *J. Mater. Chem.*, 2009, **19**, 4609–4614.
3 H. Park, K. Byeon, K. Yang, J. Cho and H. Lee, *Nanotechnology*, 2010, **21**, 355304.
4 D. Vanmaekelbergh and L. K. van Vugt, *Nanoscale*, 2011, **3**, 2783–2800.
5 J. Chang, M. Z. Ahmad, W. Wlodarski and E. R. Waclawik, *Sensors*, 2013, **13**, 8445–8460.
6 J. Chang and E. R. Waclawik, *J. Nanopart. Res.*, 2012, **14**, 1–14.
7 D. Japić, I. Djerdj, M. Marinšek and Z. C. Orel, *Acta Chim. Slov.*, 2012, **60**, 797–806.
8 I. Bilecka, L. Luo, I. Djerdj, M. D. Rossell, M. Jagodic, Z. Jaglicic, Y. Masubuchi, S. Kikkawa and M. Niederberger, *J. Phys. Chem. C*, 2011, **115**, 1484–1495.
9 L. Liao, H. B. Lu, J. C. Li, H. He, D. F. Wang, D. J. Fu, C. Liu and W. F. Zhang, *J. Phys. Chem. C*, 2007, **111**, 1900–1903.
10 G. Ambrožič, I. Djerdj, S. D. Škapin, M. Žigon and Z. Crnjak Orel, *CrystEngComm*, 2010, **12**, 1862–1868.
11 I. Djerdj, G. Garnweitner, D. Arčon, M. Pregelj, Z. Jagličić and M. Niederberger, *J. Mater. Chem.*, 2008, **18**, 5208–5217.
12 M. J. Spencer, *Prog. Mater. Sci.*, 2012, **57**, 437–486.
13 E. R. Waclawik, J. Chang, A. Ponzoni, I. Concina, D. Zappa, E. Comini, N. Motta, G. Faglia and G. Sberveglieri, *Beilstein J. Nanotechnol.*, 2012, **3**, 368–377.
14 S. Park, S. An, H. Ko, C. Jin and C. Lee, *ACS Appl. Mater. Interfaces*, 2012, **4**, 3650–3656.
15 L. Vayssieres, K. Keis, A. Hagfeldt and S. Lindquist, *Chem. Mater.*, 2001, **13**, 4395–4398.
16 H. Yang, S. Ni, X. Jiang, W. Jiang and J. Zhan, *CrystEngComm*, 2012, **14**, 6023–6028.
17 L. Zhu, Y. Zheng, T. Hao, X. Shi, Y. Chen and J. Ou-Yang, *Mater. Lett.*, 2009, **63**, 2405–2408.
18 S. Cho, J. Jang, J. S. Lee and K. Lee, *Langmuir*, 2010, **26**, 14255–14262.
19 Z. Dong, X. Lai, J. E. Halpert, N. Yang, L. Yi, J. Zhai, D. Wang, Z. Tang and L. Jiang, *Adv. Mater.*, 2012, **24**, 1046–1049.
20 X. Han, H. He, Q. Kuang, X. Zhou, X. Zhang, T. Xu, Z. Xie and L. Zheng, *J. Phys. Chem. C*, 2009, **113**, 584–589.
21 R. A. Laudise and A. A. Ballman, *J. Phys. Chem.*, 1960, **64**, 688–691.
22 J. Choy, E. Jang, J. Won, J. Chung, D. Jang and Y. Kim, *Appl. Phys. Lett.*, 2004, **84**, 287–289.
23 T. L. Sounart, J. Liu, J. A. Voigt, M. Huo, E. D. Spoerke and B. McKenzie, *J. Am. Chem. Soc.*, 2007, **129**, 15786–15793.
24 S. Xu, Y. Wei, M. Kirkham, J. Liu, W. Mai, D. Davidovic, R. L. Snyder and Z. L. Wang, *J. Am. Chem. Soc.*, 2008, **130**, 14958–14959.
25 X. Liu, M. Afzaal, K. Ramasamy, P. O. Brien and J. Akhtar, *J. Am. Chem. Soc.*, 2009, **131**, 15106–15107.
26 E. Jang, J. Won, Y. Kim, X. Chen and J. Choy, *CrystEngComm*, 2010, **12**, 3467–3470.
27 C. X. Xu, X. W. Sun, Z. L. Dong and M. B. Yu, *Appl. Phys. Lett.*, 2004, **85**, 3878–3880.
28 F. C. Meunier, *Angew. Chem., Int. Ed.*, 2011, **50**, 4053–4054.
29 F. Liao, Y. Huang, J. Ge, W. Zheng, K. Tedsree, P. Collier, X. Hong and S. C. Tsang, *Angew. Chem., Int. Ed.*, 2011, **50**, 2162–2165.
30 J. H. Zeng, B. B. Jin and Y. F. Wang, *Chem. Phys. Lett.*, 2009, **472**, 90–95.
31 A. Mclaren, T. Valdes-Solis, G. Li and S. C. Tsang, *J. Am. Chem. Soc.*, 2009, **131**, 12540–12541.

32 J. Liu, X. Chen, W. Wang, Y. Liu, Q. Huang and Z. Guo, *CrystEngComm*, 2011, **13**, 3425–3431.
33 Q. Zhao, Q. Shen, F. Yang, H. Zhao, B. Liu, Q. Liang, A. Wei and H. Yang, *Sens. Actuators, B*, 2014, **195**, 71–79.
34 Y. V. Kaneti, J. Yue, X. Jiang and A. Yu, *J. Phys. Chem. C*, 2013, **117**, 13153–13162.
35 Y. Xiao, L. Lu, A. Zhang, Y. Zhang, L. Sun, L. Huo and F. Li, *ACS Appl. Mater. Interfaces*, 2012, **4**, 3797–3804.
36 L. Xu, Y. Guo, Q. Liao, J. Zhang and D. Xu, *J. Phys. Chem. B*, 2005, **109**, 13519–13522.
37 S. Cho, J. Jang, S. Jung, B. R. Lee, E. Oh and K. Lee, *Langmuir*, 2009, **25**, 3825–3831.
38 P. Gerstel, R. C. Hoffmann, P. Lipowsky, L. P. Jeurgens, J. Bill and F. Aldinger, *Chem. Mater.*, 2006, **18**, 179–186.
39 Y. Peng, A. Xu, B. Deng, M. Antonietti and H. Cölfen, *J. Phys. Chem. B*, 2006, **110**, 2988–2993.
40 S. P. Garcia and S. Semancik, *Chem. Mater.*, 2007, **19**, 4016–4022.
41 S. Cho, H. Jeong, D. Park, S. Jung, H. Kim and K. Lee, *CrystEngComm*, 2010, **12**, 968–976.
42 R. Muñoz-Espí, G. Jeschke, I. Lieberwirth, C. M. Gómez and G. Wegner, *J. Phys. Chem. B*, 2007, **111**, 697–707.
43 L. P. Bauermann, A. del Campo, J. Bill and F. Aldinger, *Chem. Mater.*, 2006, **18**, 2016–2020.
44 S. Cho, J. Jang, J. S. Lee and K. Lee, *Langmuir*, 2010, **26**, 14255–14262.
45 N. Qin, X. Wang, Q. Xiang and J. Xu, *Sens. Actuators, B*, 2014, **191**, 770–778.
46 J. Sithole, B. D. Ngom, S. Khamlich, E. Manikanadan, N. Manyala, M. L. Saboungi, D. Knoessen, R. Nemutudi and M. Maaza, *Appl. Surf. Sci.*, 2012, **258**, 7839–7843.
47 S. Tian, F. Yang, D. Zeng and C. Xie, *J. Phys. Chem. C*, 2012, **116**, 10586–10591.
48 R. Allmann, *Z. Kristallogr., Kristallgeom., Kristallphys., Kristallchem.*, 1968, **126**, 417–426.
49 F. C. Hawthorne and E. Sokolova, *Can. Mineral.*, 2002, **40**, 939–946.
50 T. Long, S. Yin, K. Takabatake, P. Zhnag and T. Sato, *Nanoscale Res. Lett.*, 2009, **4**, 247–253.
51 S. Khamlich, A. Bello, M. Fabiane, B. D. Ngom and N. Manyala, *J. Solid State Electrochem.*, 2013, **17**, 2879–2886.
52 M. C. Hales and R. L. Frost, *J. Therm. Anal. Calorim.*, 2008, **91**, 855–860.
53 H. Chen, L. Zhu, H. Liu and W. Li, *Electrochim. Acta*, 2013, **105**, 289–298.
54 Y. Li, Y. Zou and Y. Hou, *Cryst. Res. Technol.*, 2011, **46**, 305–308.
55 C. Richard, A. Catlow, A. A. Sokol and A. Walsh, *Chem. Commun.*, 2011, **47**, 3386–3388.
56 S. Bai, T. Guo, Y. Zhao, R. Luo, D. Li, A. Chen and C. Chiun Liu, *J. Mater. Chem. A*, 2013, **1**, 11335–11342.
57 M. D. McCluskey and S. J. Jokela, *J. Appl. Phys.*, 2009, **106**, 71101.
58 M.-K. Lee and H.-F. Tu, *J. Appl. Phys.*, 2007, **101**, 126103.
59 H. Zeng, G. Duan, Y. Li, S. Yang, X. Xu and W. Cai, *Adv. Funct. Mater.*, 2010, **20**, 561–572.
60 K. T. Roro, J. K. Dangbegnon, S. Sivaraya, A. Leitch and J. R. Botha, *J. Appl. Phys.*, 2008, **103**, 53516.
61 W. Cheng, P. Wu, X. Zou and T. Xiao, *J. Appl. Phys.*, 2006, **100**, 54311.
62 C.-H. Tsai, W.-C. Wang, F.-L. Jenq, C.-C. Liu, C.-I. Hung and M.-P. Houng, *J. Appl. Phys.*, 2008, **104**, 53521.
63 X. Q. Wei, B. Y. Man, M. Liu, C. S. Xue, H. Z. Zhuang and C. Yang, *Phys. B*, 2007, **388**, 145–152.
64 G. R. Li, T. Hu, G. L. Pan, T. Y. Yan, X. P. Gao and H. Y. Zhu, *J. Phys. Chem. C*, 2008, **112**, 11859–11864.
65 O. Dulub, U. Diebold and G. Kresse, *Phys. Rev. Lett.*, 2003, **90**, 16102.
66 P. Qi, O. Vermesh, M. Grecu, A. Javey, Q. Wang, H. Dai, S. Peng and K. J. Cho, *Nano Lett.*, 2003, **3**, 347–351.
67 P. C. Chen, S. Sukcharoenchoke, K. Ryu, L. Gomez de Arco, A. Badmaev, C. Wang and C. Zhou, *Adv. Mater.*, 2010, **22**, 1900–1904.
68 Z. Gergintschew, H. Förster, J. Kostiza and D. Schipanski, *Sens. Actuators, B*, 1995, **26**, 170–173.
69 M. Grätzel, *Nature*, 2001, **414**, 338–344.
70 J. C. Belmonte, J. Manzano, J. Arbiol, A. Cirera, J. Puigcorbe, A. Vila, N. Sabate, I. Gracia, C. Cane and J. R. Morante, *Sens. Actuators, B*, 2006, **114**, 881–892.
71 Y. Zhang, J. Xu, Q. Xiang, H. Li, Q. Pan and P. Xu, *J. Phys. Chem. C*, 2009, **113**, 3430–3435.
72 N. Yamazoe, G. Sakai and K. Shimanoe, *Catal. Surv. Asia*, 2003, **7**, 63–75.
73 P. P. Sahay, *J. Mater. Sci.*, 2005, **40**, 4383–4385.
74 Y. Yan, M. M. Al-Jassim and S. Wei, *Phys. Rev. B: Condens. Matter Mater. Phys.*, 2005, **72**, 161307.
75 M. Chen, Z. Wang, D. Han, F. Gu and G. Guo, *J. Phys. Chem. C*, 2011, **115**, 12763–12773.
76 C. Wöll, *Prog. Surf. Sci.*, 2007, **82**, 55–120.
77 T. Jinkawa, G. Sakai, J. Tamaki, N. Miura and N. Yamazoe, *J. Mol. Catal. A: Chem.*, 2000, **155**, 193–200.
78 J. Xu, J. Han, Y. Zhang, Y. Sun and B. Xie, *Sens. Actuators, B*, 2008, **132**, 334–339.